Journal of Power Sources 254 (2014) 153–160

Contents lists available at ScienceDirect

Journal of Power Sources

journal homepage: www.elsevier.com/locate/jpowsour

In situ hydrothermal growth of hierarchical ZnO nanourchin for high-efficiency dye-sensitized solar cells

Yan-Zhen Zheng [a,b], Haiyang Ding [c], Yu Liu [a], Xia Tao [a,*], Guozhong Cao [d], Jian-Feng Chen [b]

[a] State Key Laboratory of Organic–Inorganic Composites, Beijing University of Chemical Technology, Beijing 100029, China
[b] Research Center of the Ministry of Education for High Gravity Engineering & Technology, Beijing University of Chemical Technology, Beijing 100029, China
[c] General Research Institute for Nonferrous Metals, Beijing 100088, China
[d] Department of Materials Science and Engineering, University of Washington, Seattle, WA 98195, USA

HIGHLIGHTS

- Hierarchical 1D ZnO nanoarchitecture is grown on a multi-scale ZnO seeded layer.
- Light harvesting and charge transport are simultaneously maximized.
- A superb photo-to-current conversion efficiency of 6.40% is obtained.

GRAPHICAL ABSTRACT

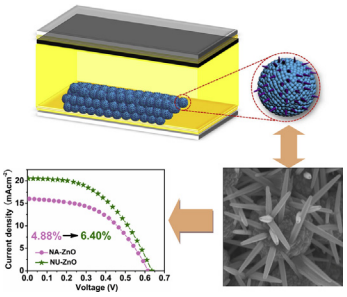

ARTICLE INFO

Article history:
Received 15 November 2013
Received in revised form
23 December 2013
Accepted 29 December 2013
Available online 4 January 2014

Keywords:
Dye-sensitized solar cell
In situ growth
Nanourchin
Zinc oxide nanocrystalline aggregate

ABSTRACT

The ability to fabricate 1D nanotexture photoanodes with a high degree of multifunctionalities by structural and morphological control still represents a vital issue towards boosting the ultimate photoelectric conversion efficiency of DSCs. In this work, we report an innovative experimental design for in-situ hydrothermal growth of hierarchical ZnO nanourchin on multi-scale ZnO (i.e. nanocrystalline aggregate) seeded layer as photoanode for use in high-efficiency DSCs. It is found that this fascinating 1D nanoarchitecture can simultaneously achieve three favorable characteristics which are generally incompatible with one another in a mono-layer photoelectrode: large dye adsorption amount, strong light scattering and direct electron transport networks, hence leading to a significant improvement of solar cell performance ranging from light harvesting capacity to electron collection efficiency. An enhanced conversion efficiency of 6.40% for hierarchical ZnO nanourchin-based DSC is achieved, with a significant efficiency improvement of 31.1% in comparison with ZnO nanocrystalline aggregate-based DSC, and also far higher than reported efficiency of pure 1D ZnO-based cell.

1. Instruction

One-dimensional (1D) nanostructured metal oxides are of great interest because of their unique physical properties that make them the most fascinating functional materials for applications in photocatalysis, gas sensors, electrochromic devices, light-emitting diodes, field emitters, and energy conversion and storage systems [1–10]. Among these applications, 1D nanoarchitectures of ZnO with direct electric pathways are particularly attractive as photoanodes of dye-sensitized solar cells (DSCs) due to their high electron mobility (~205–1000 $cm^2\ V^{-1}\ s^{-1}$), increased electron diffusion length (~100 μm), and easy tailoring of the nanostructure via a mild wet-chemical method compared with conventional TiO_2 [8,11,12]. However, the low internal surface area of simple 1D

* Corresponding author. Tel.: +86 10 6445 3680; fax: +86 10 6443 4784.
E-mail address: taoxia@yahoo.com (X. Tao).

0378-7753/$ – see front matter © 2014 Elsevier B.V. All rights reserved.
http://dx.doi.org/10.1016/j.jpowsour.2013.12.123

nanostructures constrains the energy conversion efficiency to relatively low levels i.e. 1.5% for ZnO nanowire DSC and 2.4% for ZnO nanorod DSC [8,13]. As such, nanostructures combining multi-scale hierarchical configurations have been successively developing for boosted surface area and energy conversion efficiency [14–18]. A prominent example reported by Ko et al. is the fabrication of nanoforest of hydrothermally grown hierarchical ZnO nanowires by using a simple engineering of nanocrystalline seeds [14]. They demonstrated a significant enhancement in nanowire-based cell conversion efficiency, but the full sun efficiency was still considerably low, only 2.63%, again due to insufficient surface area of the nanowire network. Therefore, how to fabricate 1D ZnO nanostructures with substantially large surface area for dye adsorption and light harvesting is believed to the key step in achieving high-efficiency DSCs. In our previous work, we reported on the synthesis of ZnO nanocrystalline aggregates (NA-ZnO) with or without doping elements and films consisting of these materials as photoanodes for ruthenium- or indoline-based DSCs [19–23]. We demonstrated that hierarchically structured ZnO electrode films possessed large internal surface area for dye adsorption and strong light-scattering for optical absorption. Considering that 1D ZnO nanoarchitectures can be readily obtained from the single-scale ZnO seeds via a wet chemical process, we thus imagine if there is any possibility of using NA-ZnO with large surface area as a seed layer to fabricate hierarchical 1D electrode films and consequently to boost power conversion efficiency of DSCs.

Herein, we report an innovative experimental design to photoanode tailoring by which the photovoltaic performance of DSCs can be boosted. Our strategy exploits a new class of hierarchical ZnO 1D nanoarchitecture photoanode film synthesized for the first time via in-situ hydrothermal growth on a multi-scale structured seed i.e. NA-ZnO (see Scheme 1). In schematic diagram, the most fascinating model for illustrating the novel multifunctional 1D nanostructure is perhaps a sea urchin, in which each nanoparticulate in an aggregate is analogous to the foot of urchin spine and omni-directional nanorod resembles the spine. In contrast to a zigzag electron transport pathway occurring in NA-ZnO photoanode, a directed electron pathway along the long axis of the nanorods in a randomly intercalated 3D structure may be discerned in hierarchical ZnO nanourchin (NU-ZnO) photoanode (Scheme 1). In such hierarchical 1D ZnO nanourchin, the primary submicrometer-sized NA-ZnO seeded layer that makes up of nanocrystallites exhibits large internal surface area and strong light-scattering property. Apart from this, we hypothesize that the ZnO nanorods in-situ grown on the surface of NA-ZnO may endow two extra prominent advantages to this architecture i.e. eminent charge transport and strengthened light-scattering effect (see Fig. S1). Various morphological characterizations and photovoltaic performance measurements towards the nanourchin-like ZnO photoanode verified the hypothesis. As a result, an enhanced conversion efficiency of 6.40% for NU-ZnO-based DSC was achieved, with a significant efficiency improvement of 31.1% in comparison with NA-ZnO-based DSC, and also far higher than reported efficiency of pure 1D ZnO-based cell.

2. Experimental

2.1. Materials

Anhydrous lithium iodine (LiI), Iodide (I_2), 1, 2-dimethyl-3-propylimidazolium iodide (DMPII), Zinc acetate dihydrate ($(CH3COO)_2Zn$) and chloroplatinic acid (H_2PtCl_6) were purchased from Sigma. Zinc nitrate hexahydrate ($Zn(NO_3)_2 \cdot 6H_2O$) and hexamethylenetetramine ($(CH_2)_6N_4$) and 4-tert-butylpyridine (TBP) were received from Aladdin. Acetone, diethylene glycol ($(HOCH_2CH_2)_2O$), sodium hydroxide (NaOH), acetonitrile and anhydrous ethanol (analytical grade purity) were obtained from Beijing Chemical Works and were used without further purification. Indoline dye D205 was obtained from Shanghai Green Technology Co. Ltd. All solutions used in this work were prepared with 18.2 MΩ cm^{-1} water produced by a reagent water system (Easy pure II, Barnstead).

2.2. Preparation of NU-ZnO photoanodes and DSCs

The synthesis of NU-ZnO on conductive substrate was performed following a simple two-step method. NA-ZnO was synthesized by the solvothermal process of zinc salt in polyol medium at 160 °C [19,20,22,23]. NA-ZnO films were constructed onto the FTO and ITO (for XRD and SEM characterization) by means of a doctor-blade method following by calcination at 350 °C for 60 min to obtain the ZnO seeded layer. NU-ZnO photoanodes were prepared by suspending the as-prepared NA-ZnO seeded substrate in a

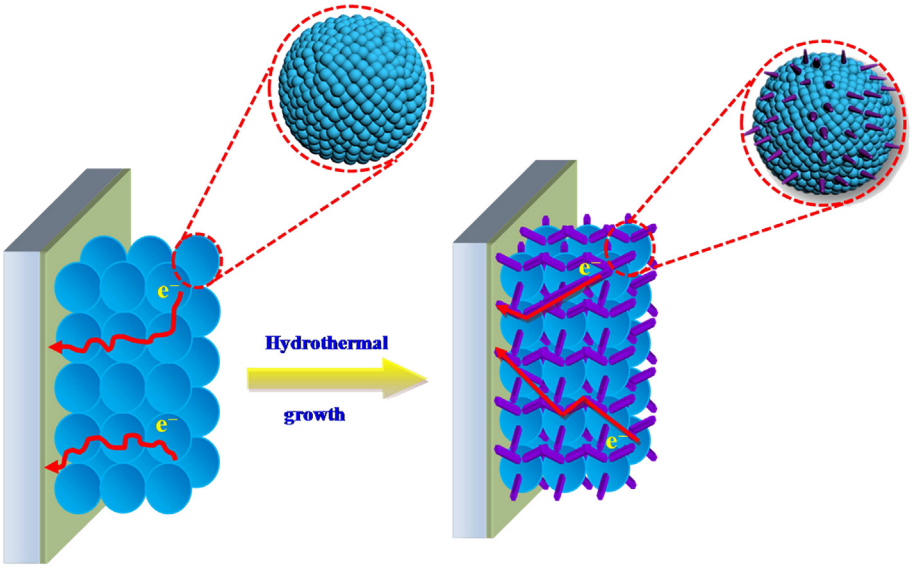

Scheme 1. In-situ preparation of NU-ZnO film and electron diffusion transport in the NA-ZnO film and NU-ZnO film; and schematic diagrams that illustrate the microstructure of aggregated ZnO and nanourchin-like ZnO.

100 mL Teflon-lined stainless steel autoclave filled with 60 mL of aqueous growth solution of $Zn(NO_3)_2 \cdot 6H_2O$ and $CH_2)_6N_4$ with three concentration ratios as follows: 1) 10 mM: 10 mM, 2) 20 mM: 20 mM and 3) 40 mM: 40 mM. Then, the reaction was conducted at 91.5 °C for 3 h. After growth, the substrate was removed from the autoclave and rinsed thoroughly in ethanol and distilled water to remove any residual reactants and dried in air. Three NU-ZnO films prepared in growth solutions with three different concentrations were labeled as NU-ZnO(1), NU-ZnO(2) and NU-ZnO(3). This two-step preparation process is a simple, low-temperature and environmentally benign route to form NU-ZnO with controllable length and density of nanorods on arbitrary substrates [21,24]. For comparison, NA-ZnO film with identical thickness was also fabricated.

For dye adsorption, the resulting NU-ZnO film was immersed into a 0.5 mM D205 and 1.0 mM chenodeoxycholic acid in acetonitrile/tert-butyl alcohol (V/V = 1: 1) for approximately 50 min at 60 °C. The Pt-coated thin films served as counter electrodes were constructed by dropping 0.35 mM H_2PtCl_6 solution on the FTO, followed by annealing at 400 °C for 15 min in air. The dye-absorbed NU-ZnO film and Pt counter electrode were assembled with a 25 μm gap using a Surlyn space (Dupont). The electrolyte composition was 0.03 M I_2, 0.5 M 1,2-dimethyl-3-propyl-imidazoliumiodide (DMPII), and 0.5 M tertbutylpyridine in acetonitrile. The active area of the resulting cell exposed in light was approximately 0.25 cm^2.

2.3. Characterization

The morphology and microstructure of the NU-ZnO film was examined using a JEOL JSM-6701 F field emission scanning electron microscope (SEM) and a JEOL JEM-3010 transmission electron microscopy (TEM). The crystalline structure of the NU-ZnO film/ITO substrate was characterized using an X-ray diffractometer (XRD) (Rigaku, D/max 2500 VB2+/PC), in 2θ range from 10° to 70° with CuKα radiation (λ = 0.15406 nm) operated at 40 mA and 40 kV. The light absorption and reflectance properties of the samples were investigated by UV–visible light absorption/diffused reflectance spectrometry (Lambda 950, PerkinElmer). The photoelectrochemical characterization of DSCs was performed using electrochemical station (CHI660C, Shanghai) under simulated AM 1.5 sunlight illumination with 100 mW cm^{-2} light output. A 1000 W xenon lamp (Thermo Oriel, America) served as the light source. The electrochemical impedance spectroscopy (EIS) measurement was performed on an electrochemical workstation (Zennium Zahner, Germany). EIS test was recorded under one-sun illumination at a V_{oc} with ac amplitude of 10 mV and a frequency ranging from 10^{-1} to 10^5 Hz. Monochromatic light in the range of 400–800 nm was obtained by using a series of filters and the incident photon-to-current conversion efficiency (IPCE) measurement was performed on a Keithley Model 2000 Source Meter.

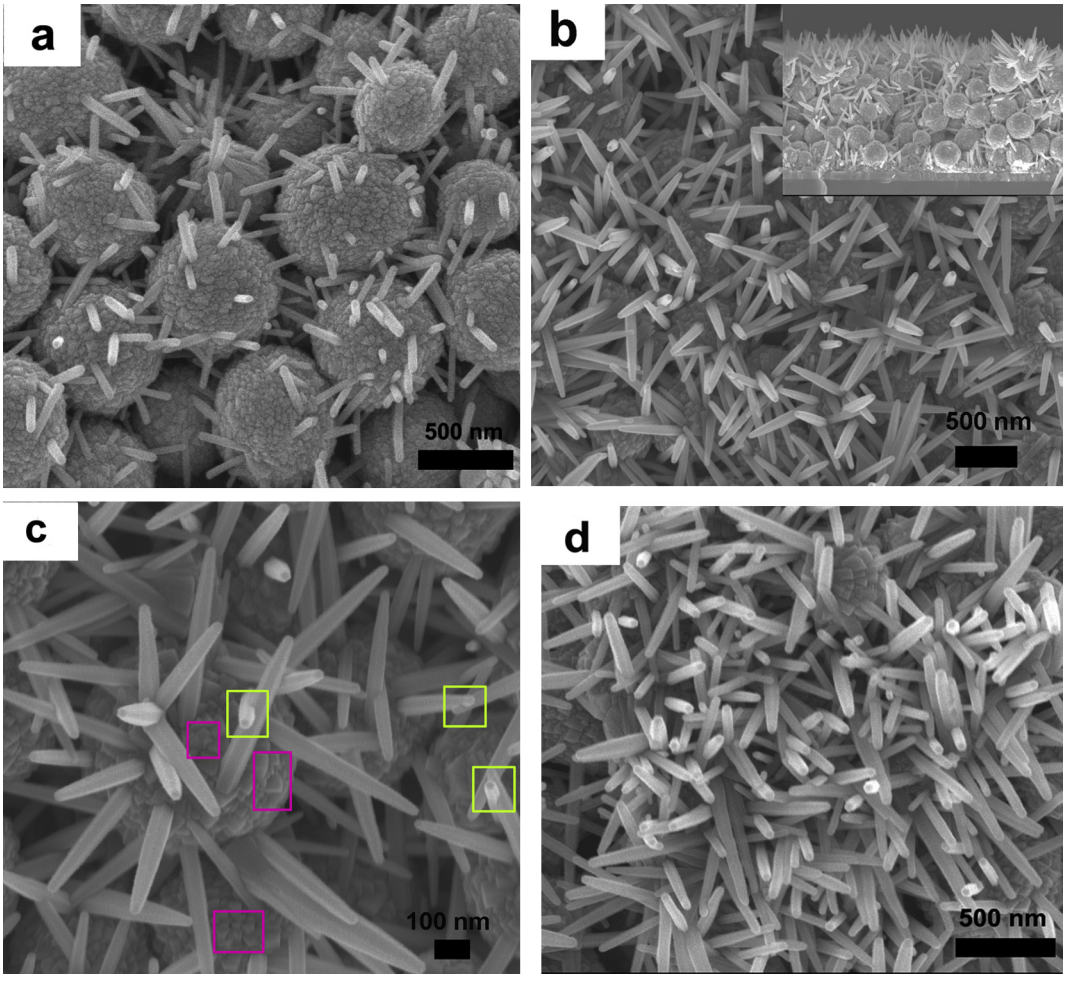

Fig. 1. Top-view SEM images of (a) NU-ZnO(1), (b & c) NU-ZnO(2), and (d) NU-ZnO(3). Inset of image b showing cross-section SEM image of a thin NU-ZnO (2) film.

3. Results and discussion

3.1. Morphological characterization

Top-view SEM images of NU-ZnO(1–3), as shown in Fig. 1a–d and Fig. S2, exhibit that omni-directional rods are grown on the surface of NA-ZnO seeded film (Fig. S3). From top-view SEM image of NU-ZnO(1) (Fig. 1a), sparse nanorods grown on the surface of aggregates in a diluted Zn-precursor growth solution can be easily visualized to be very short in length. As for NU-ZnO(2), the nanorods with higher density and length could be found in Fig. 1b & c and Fig. S2. The measured nanorod number density is $\sim 6 \times 10^7$ cm^{-2} for NU-ZnO(2). While given sufficient formulated nutrient solution, nanocrystallite seeds are apt to blossom into nanorods with higher density and length (NU-ZnO(3), Fig. 1d). Also, from the cross-sectional SEM image of thin NU-ZnO film (inset of Fig. 1b), it can be observed that the inherent characteristics of nanorods and nanocrystallites can be well preserved. It shows that the nanorods spread in NU-ZnO film from bottom to top, including on the top of the film and the limited space within the film. A large difference between nanorods grown on NA-ZnO seeded substrate versus nanocrystalline-seeded substrate lies in the varying orientation of nanorods [14,17]. Such omni-directional nanorods may not only increase light-harvesting efficiency by scattering enhancement and trapping arising from (sub-)micron-sized hierarchical nanourchin-like structure but also form free spaces within ZnO nanoarchitecture in favor of the full infiltration of electrolyte. A high-magnification SEM image shows that some nanorods remain growth along *c* axis even though there exists intersection between two rods (see green marks in Fig. 1c in the web version) and some nanocrystallite seeds are beginning to sprout on the aggregates (see rosy marks in Fig. 1c). Each nanorod looks like a nanotower with an uneven width change from the bottom to the top. According to the literature [25], the (0001) planes of ZnO possess higher surface energy than the (1000) planes. The growth velocity of the crystal (0001) planes with higher surface energy is faster than that of the (1000) planes. As a consequence, the (1000) planes with slower growth velocity gradually dominate the morphology of crystal in hydrothermal process, and hence leading to the formation of nanorod with the uneven width along its length. Indeed, the dominating (1000) planes have been demonstrated to be able to significantly improve the rate of electron injection from photoexcited dye into the nanorod film compared with the commonly used nanoparticulate film, which accordingly may be considered to

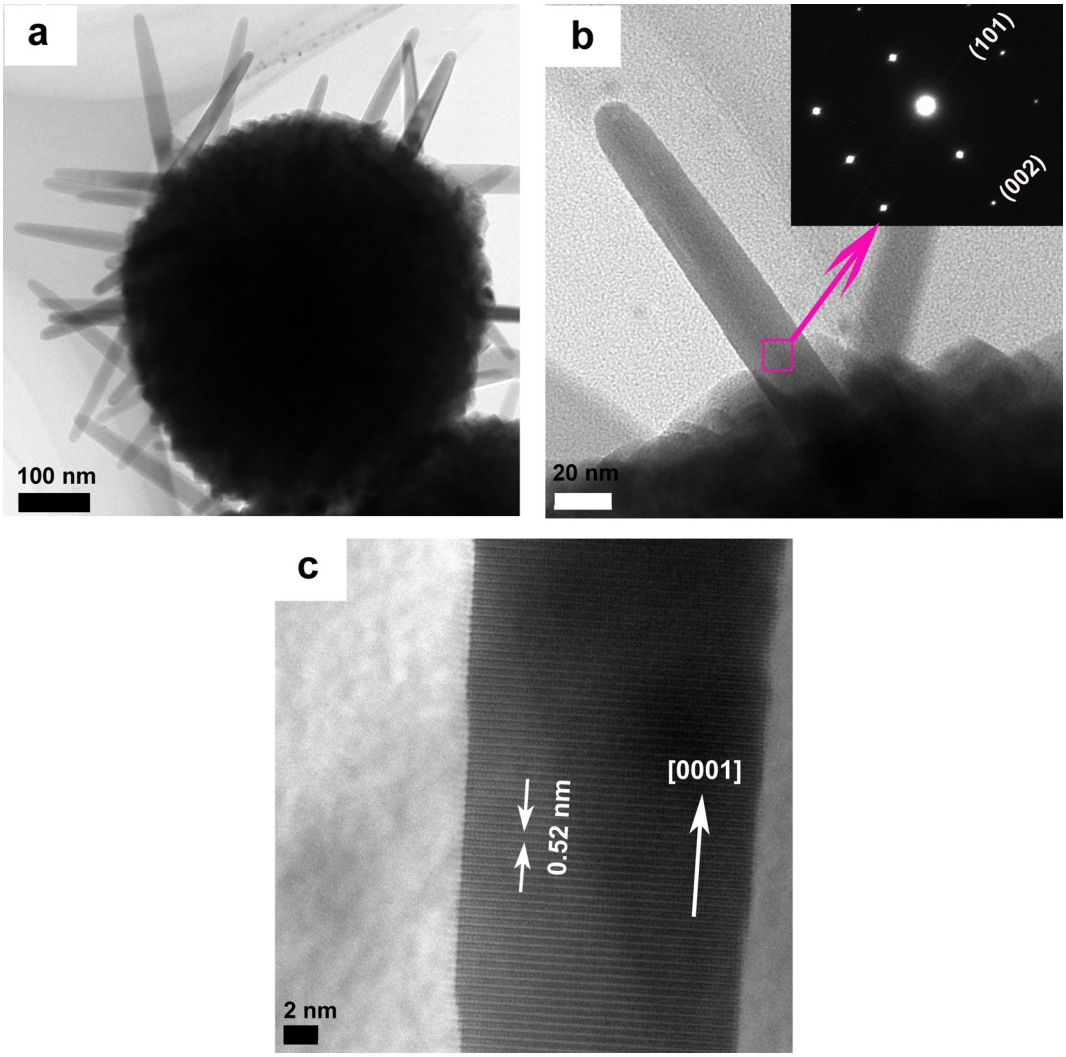

Fig. 2. (a) High-resolution TEM image of NU-ZnO; (b & c) High-resolution TEM images of the nanorod grown on NU-ZnO. Inset of image b showing selected area electron diffraction pattern of a nanorod.

compensate the weak light-absorption arising from insufficient dye uptake of nanorods to some extend [8].

To further examine the nanometer-scale features of NU-ZnO, high resolution TEM characterization was also performed. Fig. 2a displays a single nanourchin (NU-ZnO(2)) consisting of submicron-sized nanocrystalline aggregate and nanorods. Note that nanorods are 15–30 nm in diameter and 50–250 nm in length. A higher magnification image clearly shows that a nanorod is in-situ grown on the surface of aggregate (Fig. 2b). The well-defined spots of the corresponding selected area electron diffraction (SAED) pattern (inset of Fig. 2b) indicate a single-crystalline structure of ZnO and a preferred growth direction along the *c* axis. The enlarged detail of an individual nanorod (Fig. 2c) shows an interplane spacing of 0.52 nm and this also implies the growth direction of the nanorod along [0001]. As a matter of fact, a single-crystalline structured photoanode material obtained via hydrothermal growth process has been demonstrated to possess fewer surface and bulk defects in comparison with disordered nanoparticulates, which allows assisting carrier collection by separating injected electrons from the surrounding electrolyte and sweeping them towards the collecting electrode [7,8,26].

3.2. X-ray diffraction patterns

Fig. 3 shows XRD patterns of all the ZnO films and all diffraction peaks can be well indexed to be wurtzite ZnO (hexagonal phase, space group P63mc, ICDD No. 36-1451). The hexagonal cell values were calculated as $a = 0.3253$ nm, $c = 0.5207$ nm, in excellent agreement with those of ICDD No. 36-1451 ($a = 0.3250$ nm, $c = 0.5207$ nm). It is noticeable that as the concentration of ZnO-precursor solution increases, the diffraction intensity of typical ZnO peak (002) at $2\theta = 34.4^{\circ}$ strengthens accordingly, indicating the formation of ZnO nanorods predominantly along the [0001] direction of a hexagonal singe crystal [27].

3.3. Photovoltaic performance

The photovoltaic properties for DSCs based on NA-ZnO and NU-ZnO(1–3) photoanodes were measured under the AM 1.5 sunlight illumination (100 mW cm^{-2}), as shown in Fig. 4. Table 1 summarizes the photoelectric characteristics of the four cells. It should be pointed out that the thickness of all the ZnO-based films using for photovoltaic performance characterization is controlled to be identical to be 12 ± 0.5 μm. The NA-ZnO cell shows a short-circuit current density (J_{sc}) of 16.0 mA cm^{-2}, an open-circuit voltage (V_{oc}) of 0.615 V and a conversion efficiency (η) of 4.88%. In comparison

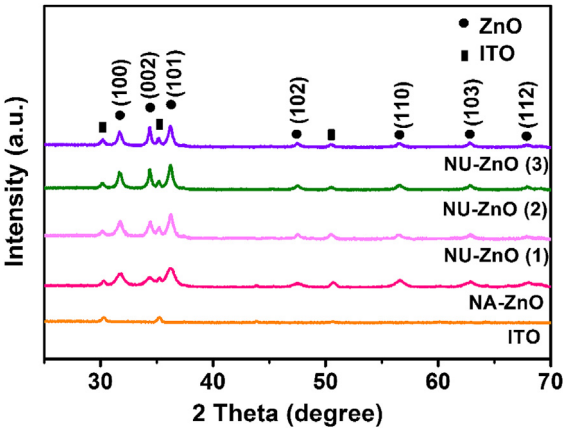

Fig. 3. XRD patterns of NA-ZnO and NU-ZnO(1–3) films.

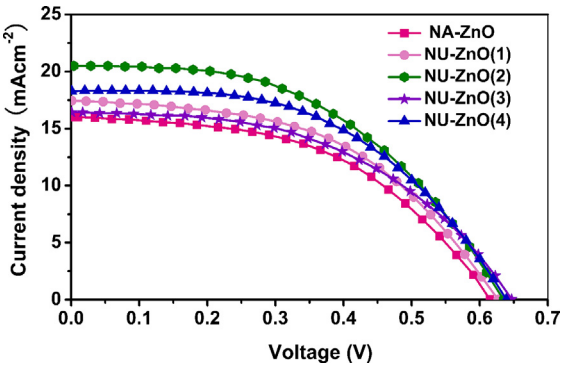

Fig. 4. *I–V* curves of DSCs based on NA-ZnO and NU-ZnO(1–4) photoanodes.

with NA-ZnO cell, the J_{sc} and V_{oc} of NU-ZnO(1) cell enhance to 17.5 mA cm^{-2} and 0.627 V, respectively, and thus leading to a η of 5.42%. Impressively, the efficiency of NU-ZnO(2) cell is further enhanced to 6.40%, with a highest J_{sc} of 20.5 mA cm^{-2} and V_{oc} of 0.635 V. The highest η of NU-ZnO(2) cell corresponds to a 31.1% increment of NA-ZnO cell. However, unfortunately, J_{sc} and η of NU-ZnO(3) cell significantly decrease to 16.4 mA cm^{-2} and 5.20%, respectively. In order to precisely determine the optimized Zn-precursor concentration for attaining a high efficiency, a DSC based on an NU-ZnO film that prepared in 30 mM aqueous growth solution was also assembled and characterized, resulting in a η of 5.97% (see NU-ZnO(4)). The discrepancy of photovoltaic performance of the NA-ZnO and NU-ZnO cells is thought to be closely related to the tailored nanorod density and length. On one hand, lengthened and dense nanorods grown on the surface of NA-ZnO may increase the superficial size of NU-ZnO, resulting in an enhanced light scattering [14]. On the other hand, in-situ grown nanorods may act as the bridges between nanocrystalline aggregates to construct network interconnections within NU-ZnO film and thus offer more pathways for electron transport (see inset of Fig. 1b) [28]. However, further increase in diameter and length would inevitably cause the decrease in surface area and dye loading of the film, hence leading to the decrease of η. The detailed photoelectric characteristics of the photoanode films including light harvesting efficiency and the electron transport property arising from tailored nanorods will be discussed below.

3.4. Dye-uptake and reflectance spectra

For NU-ZnO was in-situ grown tightly onto FTO substrate, the resulting NU-ZnO film is difficult to be scraped off the substrate, with closely packed ZnO architecture. Also, due to the presence of rigid FTO substrate accurate measurement of the surface area of the NU-ZnO film is hard to achieve. Thus, the surface area of the NU-ZnO film is not given herein. Since a key performance of photoanode i.e. dye uptake is predominantly dependent on the surface area of the photoanode film, the change in surface area of the ZnO

Table 1
Comparison of J_{sc}, V_{oc}, ff, η, and dye loading amount for DSCs based on NA-ZnO and NU-ZnO(1–4).

Cells	J_{sc} (mA cm^{-2})	V_{oc} (V)	ff (%)	η (%)	Dye-uptake (nmol cm^{-2})
NA-ZnO	16.0	0.615	49.6	4.88	98
NU-ZnO(1)	17.5	0.627	49.4	5.42	92
NU-ZnO(2)	20.5	0.635	49.2	6.40	81
NU-ZnO(3)	16.4	0.647	48.8	5.20	59
NU-ZnO(4)	18.2	0.639	51.3	5.97	74

film may be indirectly expressed by dye adsorption amount variations [14,29]. The amount of dye loading in all ZnO films is summarized in Table 1. Compared with NA-ZnO film (98 nmol cm^{-2}), dye loading amount in photoanode films decreases from NU-ZnO(1) (92 nmol cm^{-2}) to NU-ZnO(3) (59 nmol cm^{-2}). The decrease in dye uptake can be ascribed to the presence of low-surface-area nanorods and disappearance of a fraction of large-surface-area nanoparticles in the NU-ZnO film. But the dye uptake of NU-ZnO(1–3) films still remains in the same magnitude as that of NA-ZnO film. To investigate the light-scattering effect of the NU-ZnO, UV–vis reflectance spectra of films were measured (Fig. 5). Apparently, NU-ZnO(1–3) films have higher reflectance in the wavelength range of 400–800 nm than NA-ZnO. As usual, high reflectance means better light-scattering ability [22,23]. The light scattering will inevitably affect the transport behavior of light through changing the light path and/or extending the travel distance within the photoelectrode film (see the light transport path in NU-ZnO film, Fig. S1), and hence provide the photons with more opportunities to be absorbed by the dye molecules. As a result, the light-harvesting efficiency of the nanourchin-like NU-ZnO framework film is greatly enhanced.

3.5. EIS analysis

EIS analysis was also performed to study the effect of omni-directional nanorods in-situ grown on ZnO aggregates on the charge transport property and the light-to-electric conversion efficiency of DSCs. Fig. 6a and b displays the Nyquist and Bode plots of impedance spectra of DSCs assembled by NA-ZnO and NU-ZnO(1–3). Generally, three semicircles presented in the Nyquist plot can be assigned to the redox reaction at the Pt counter electrode/electrolyte interface at high frequency (in the kHz range), the electron transfer at the oxide layer/dye/electrolyte interface at medium frequency (in the $1–10^3$ Hz) together with the Warburg diffusion process of I^-/I_3^- in the electrolyte at low frequency (<1 Hz range) [30–32]. In our work, the EIS spectra exhibit two distinguishable semicircles, and the low-frequency semicircle related to diffusion resistance for the redox couple is virtually overlapped with the medium-frequency semicircle owing to the relatively short distance for I^- ion diffusion within the thin 25 μm-thick spacer [28]. As we know, the extent of electron transport in the photoanode can be judged by the impedance, which is determined from the central arc diameter of medium-frequency semicircle. From Fig. 6a, it can be seen that under one-sun illumination, a decrease trend of the diameter in a sequence of NA-ZnO > NU-ZnO(1) > NU-ZnO(2) > NU-ZnO(3) cells, suggesting a less

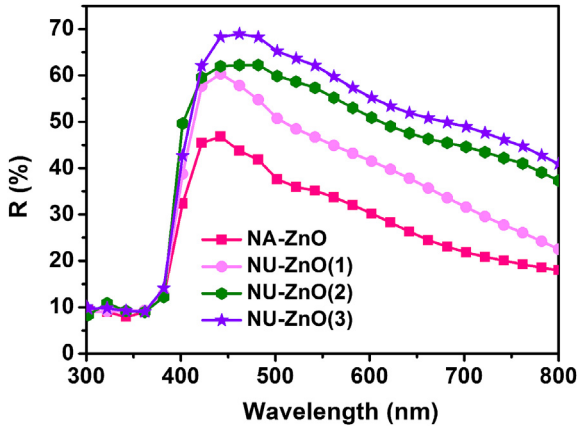

Fig. 5. Diffused reflectance spectra of NA-ZnO and NU-ZnO(1–3) photoanodes.

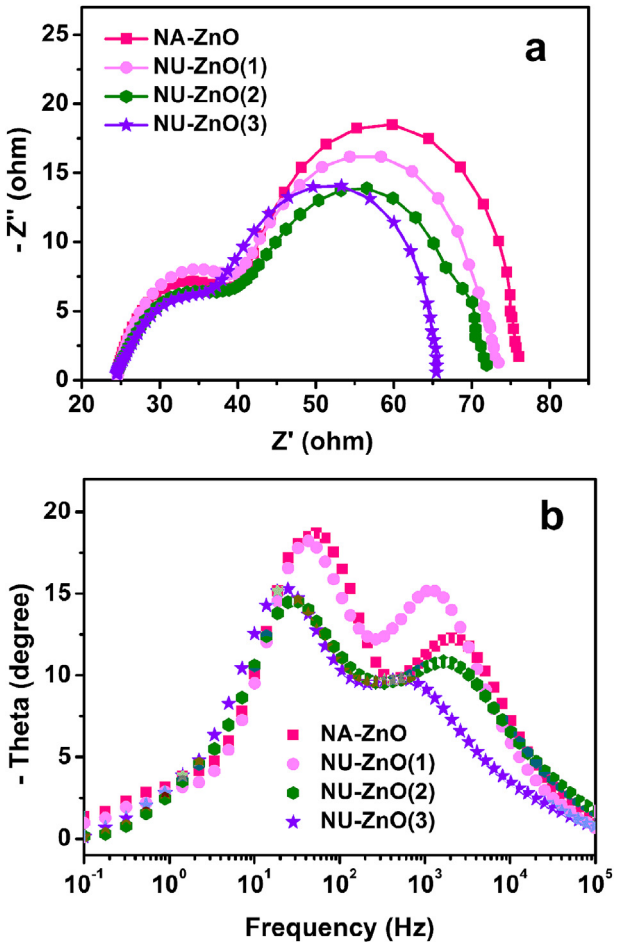

Fig. 6. (a) Nyquist and (b) Bode plots of DSCs based on NA-ZnO and NU-ZnO(1–3) photoanodes.

impedance and a higher electron collection efficiency in the NU-ZnO-based DSCs. This is mainly originating from the direct electron transport pathway and the decreased intercrystalline contacts between grain boundaries in the presence of omni-directional ZnO nanorods [31]. Besides, more free electrons that are produced owing to the excellent light-scattering effect at the NU-ZnO surfaces also contribute to the charge transport at the photoanode [33].

Bode plots (Fig. 6b) exhibit two main frequency peaks at the ranges of $10^1–10^2$ Hz and $10^3–10^4$ Hz, respectively. The two peaks correspond to the charge transfer processes at different interfaces in the interior of DSCs. Notably, the maximum frequency (f_{max}) peaks of NU-ZnO(1–3) in the intermediate frequency regime ($10^1–10^2$ Hz) are lower than that of NA-ZnO. The electron lifetime (τ_e) of injected electrons in ZnO films is determined by f_{max} value, where $\tau_e = 1/(2\pi f_{max})$ [34]. The characteristic f_{max} of the intermediate frequency regime are located at 53.5 Hz for NA-ZnO, 42.8 Hz for NU-ZnO(1), 32.4 Hz for NU-ZnO(2), and 27.4 Hz for NU-ZnO(3), respectively. Correspondingly, electron lifetime shows an increase trend in a sequence of NA-ZnO < NU-ZnO(1) < NU-ZnO(2) < NU-ZnO(3) cells. This means that with the increase of length and density of nanorods, more produced electrons can diffuse further without recombination with redox electrolyte at ZnO/dye/electrolyte interface and trapping within the film [35]. A prolonged electron lifetime and decreased recombination can be explained by the higher electron mobility through single-crystalline ZnO nanorods linked to nanocrystalline aggregates.

3.6. IPCE spectra

IPCE spectra of DSCs based on the four photoanodes provide further evidence for the excellent electron transport property of hierarchical nanourchin architecture. Fig. 7 shows IPCE spectra of DSCs with NA-ZnO and NU-ZnO(1–3) as a function of the illuminated wavelength. Strong photoactivity for both photoanodes is observed in the visible light region from 470 nm to 600 nm, coinciding with the absorption maximum wavelength of the D205 dye. In contrast to NA-ZnO cell, NU-ZnO(1–3) cells show higher photoresponse in the entire wavelength region, and the maximum IPCE value of NU-ZnO(2) cell is 80.1% at 500 nm. The value of calculated J_{sc} by integrating the IPCE spectra over the spectral distribution of the standard AM 1.5 solar photon flux (I_s) is ca. 18 mA cm^{-2}, which is smaller than that of the measured J_{sc} value (20.5 mA cm^{-2}). The higher J_{sc} obtained illumination intensity (I–V measurement) than at low monochromatic light intensity (IPCE measurement) [34], and ii) the counter electrode provides additional light absorption and scattering of the incident light, resulting in the higher measured J_{sc} [36,37].

In general, IPCE is related to the absorptivity, the injection efficiency and the electron collection efficiency. The absorptivity is proportional to dye loading of photoanodes. In our system, NU-ZnO(1–3) cells show a relatively low dye adsorption amount compared with NA-ZnO cell as mentioned above. Thus, higher IPCE for NU-ZnO(1–3) cells may be ascribed to the latter two aspects. On one hand, the enhancement of IPCE in NU-ZnO(1–3) cells may be the result of improved electron injection through the (1000) facets of the nanorod/dye interface as compared to the multitude of crystal facets presented at the nanoparticle surfaces [8]. On the other hand, the nanorods grown on the nanocrystalline aggregates may bridge grain boundaries between neighbor nanoparticles and thus enhance the electron transfer within the photo-to-electron conversion process, and finally enhancing electron collection efficiency [35].

Based on the above characterizations and data analysis, NU-ZnO(2) cell shows a noteworthy improvement in the J_{sc} and η in comparison with NA-ZnO cell. This may be explained as a consequence of excellent light-scattering capacity (see Fig. 5) and electron transport property (see Fig. 6a and b). Furthermore, the omnidirectional ZnO nanorods in the NU-ZnO(2) electrode film provide continuous and directional electron transfer pathways (see Scheme 1 and Fig. 1) to enhance the amount of electrons that reach the electrode, and hence leading to a high electron collection efficiency (see Fig. 7). All aforementioned favorable features in relation to NU-ZnO(2) cell may lead to the highest J_{sc} and η.

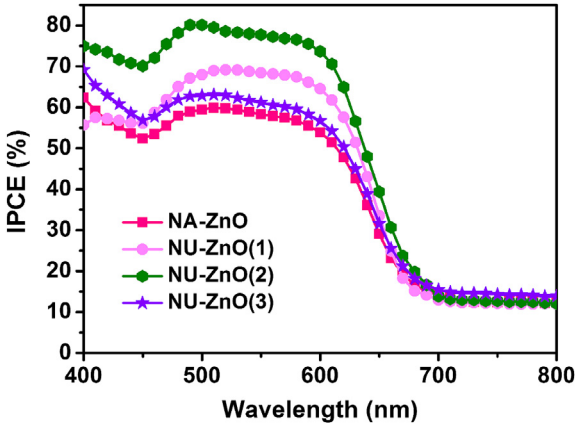

Fig. 7. IPCE spectra of DSCs based on NA-ZnO and NU-ZnO(1–3) photoanodes.

4. Conclusions

In summary, we report in situ growth of NU-ZnO on a multiscale structured nanocrystalline aggregate seeded film via a simple all-solution processed hydrothermal method incorporating a doctor blade step and its implementation as a photoanode of DSC. Fine adjustment of the structure and morphology of NU-ZnO made it feasible to simultaneously maximize the key features of a photoelectrode, which are generally incompatible with one another: large dye adsorption, strong light scattering and fast electron transport. A photo-to-electric conversion as high as 6.40% was reported for the NU-ZnO-based cell and a consistent improvement was evaluated with respect to a reference photoanode made from NA-ZnO. Further optimizing hydrothermal time as well as the size and morphology of nanocrystalline aggregates is anticipated to be able to increase conversion efficiency of urchin-like structured ZnO-DSCs. This work may open up new opportunities for fabricating high efficiency DSCs based on structural and morphological design and manipulation of hierarchical semiconductor 1D nanoarchitecture.

Acknowledgments

This work was supported financially by National Nature Science Foundation of China (NSFC) (21176019, 21121064, 51004017), the Fundamental Research Funds for the Central Universities (ZZ) and 863 Project (2013AA031901).

Appendix A. Supplementary data

Supplementary data related to this article can be found at http://dx.doi.org/10.1016/j.jpowsour.2013.12.123.

References

[1] P. Roy, S. Berger, P. Schmuki, Angew. Chem. Int. Ed. 50 (2011) 2904–2939.
[2] J. Xu, W. Zhang, Z. Yang, S. Ding, C. Zeng, L. Chen, Q. Wang, S. Yang, Adv. Funct. Mater. 19 (2009) 1759–1766.
[3] J.-Z. Chen, W.-Y. Ko, Y.-C. Yen, P.-H. Chen, K.-J. Lin, ACS Nano 6 (2012) 6633–6639.
[4] H. Guo, Z. lin, Z. Feng, L. Lin, J. Zhou, J. Phys. Chem. C 113 (2009) 12546–12550.
[5] J. She, Z. Xiao, Y. Yang, S. Deng, J. Chen, G. Yang, N. Xu, ACS Nano 2 (2008) 2015–2022.
[6] X. Yang, A. Wolcott, G. Wang, A. Sobo, R.C. Fitzmorris, F. Qian, J.Z. Zhang, Y. Li, Nano Lett. 9 (2009) 2331–2336.
[7] Y. Qiu, W. Chen, S. Yang, Angew. Chem. Int. Ed. 122 (2010) 3757–3761.
[8] M. Law, L.E. Greene, J.C. Johnson, R. Saykally, P. Yang, Nat. Mater. 4 (2005) 455–459.
[9] X.L. Zhang, Z. Zhang, F. Huang, P. Bäuerle, U. Bach, Y.-Bing Cheng, J. Mater. Chem. 22 (2012) 7005–7009.
[10] L.-Y. Chen, Y.-T. Yin, Nanoscale 5 (2013) 1777–1780.
[11] Q. Zhang, C.S. Dandeneau, X. Zhou, G. Cao, Adv. Mater. 21 (2009) 4087–4108.
[12] A.I. Hochbaum, P. Yang, Chem. Rev. 110 (2010) 527–546.
[13] M. Guo, P. Diao, X. Wang, S.M. Cai, J. Solid State Chem. 178 (2005) 3210–3215.
[14] S.H. Ko, D. Lee, H.W. Kang, K.H. Nam, J.Y. Yeo, S.J. Hong, C.P. Grigoropoulos, H.J. Sung, Nano Lett. 11 (2011) 666–671.
[15] H.-M. Cheng, W.-H. Chiu, C.-H. Lee, S.-Y. Tsai, W.-F. Hsieh, J. Phys. Chem. C 112 (2008) 16359–16364.
[16] J.B. Baxter, E.S. Aydil, Sol. Energy Mater. Sol. Cells 90 (2006) 607–622.
[17] C.Y. Jiang, X.W. Sun, G.Q. Lo, D.L. Kwong, J.X. Wang, Appl. Phys. Lett. 90 (2007) 263501–263503.
[18] N. Memarian, I. Concina, A. Braga, S.M. Rozati, A. Vomiero, G. Sberveglieri, Angew. Chem. Int. Ed. 50 (2011) 12321–12325.
[19] Y.-Z. Zheng, X. Tao, L.-X. Wang, H. Xu, Q. Hou, W.-L. Zhou, J.-F. Chen, Chem. Mater. 22 (2010) 928–934.
[20] Y.-Z. Zheng, X. Tao, Q. Hou, D.T. Wang, W.L. Zhou, J.-F. Chen, Chem. Mater. 23 (2011) 3–5.
[21] Y. Ren, Y.-Z. Zheng, J. Zhao, J.-F. Chen, W. Zhou, X. Tao, Electrochem. Commun. 16 (2012) 57–60.
[22] T.P. Chou, Q.F. Zhang, G.E. Fryxell, G.Z. Cao, Adv. Mater. 19 (2007) 2588–2592.
[23] Q.F. Zhang, T.P. Chou, B. Russo, S.A. Jenekhe, G.Z. Cao, Adv. Funct. Mater. 18 (2008) 1654–1660.
[24] X.-H. Lu, Y.-Z. Zheng, J. Zhao, J.-F. Chen, X. Tao, Electrochim. Acta 90 (2013) 649–655.

[25] Y. Tong, Y. Liu, L. Dong, D. Zhao, J. Zhang, Y. Lu, D. Sheng, X. Fan, J. Phys. Chem. B 110 (2006) 20263–20267.
[26] S.H. Kang, S.-H. Choi, M.-S. Kang, J.-Y. Kim, H.-S. Kim, T. Hyeon, Y.-E. Sung, Adv. Mater. 20 (2008) 54–58.
[27] H. Yang, Y. Song, J. Ma, D. Chen, S. Mai, H. Zhao, Cryst. Growth Des. 8 (2008) 1039–1043.
[28] Y. Bai, H. Yu, Z. Li, R. Amal, G.Q. Lu, L. Wang, Adv. Mater. 24 (2012) 5850–5856.
[29] Y.-H. Sung, W.-P. Liao, D.-W. Chen, C.-T. Wu, G.-J. Chang, J.-J. Wu, Adv. Funct. Mater. 22 (2012) 3808–3814.
[30] J. Qian, P. Liu, Y. Xiao, Y. Jiang, Y. Cao, X. Ai, H. Yang, Adv. Mater. 21 (2009) 3663–3667.
[31] K. Park, Q.F. Zhang, B.B. Garcia, G.Z. Cao, J. Phys. Chem. C 115 (2011) 4927–4934.
[32] Q. Wang, J.-E. Moser, M. Grätzel, J. Phys. Chem. B 109 (2005) 14945–14953.
[33] K. Zhu, N.R. Neale, A. Miedaner, A.J. Frank, Nano Lett. 7 (2007) 69–74.
[34] K.S. Kim, H. Song, S.H. Nam, S.-M. Kim, H. Jeong, W.B. Kim, G.Y. Jung, Adv. Mater. 24 (2012) 792–798.
[35] D.S. Kim, S.-Y. Kwak, Appl. Catal. A 323 (2007) 110–118.
[36] Z. Yang, C.-Y. Chen, C.-W. Liu, C.-L. Li, H.-T. Chang, Adv. Energy Mater. 1 (2011) 259–264.
[37] T. Ma, M. Akiyama, E. Abe, I. Imai, Nano Lett. 5 (2005) 2543–2547.